Electronic Support information

Materials and Methods

Photolithography. Microchambers were fabricated using optical lithography [1]. A layer of SU8 negative photoresist (Microchem) was spincoated on a #1 glass cover slip (Menzel, Germany). To ensure good adhesion of the SU8 film, the glass substrates were cleaned with Base Piranha (water, 30% NH_4OH, and 30% H_2O_2 in a 5:1:1 volume ratio) at 75^{o}C for 15 minutes followed by rinsing in MilliQ water and then 2-propanol. Prior to use, the substrates were dried with a stream of nitrogen and subjected to a dehydration bake for 5 minutes at 200^{o}C on a hotplate. The thickness of the SU8 layer, which sets the microchamber depth, was varied by using photoresists of different viscosities (type 2005 for 5 µm; type 2010 for 10 µm; type 2025 for 20 µm; type 3025 for 30 µm) and by using a spinning speed of either 2000 or 3000 rpm on a Delta 80 Spincoater. The coated substrate was baked for 15 min at 65^{o}C and another 15 min at 95^{o}C on a hotplate. The coverslip was then exposed to ultraviolet light (365 nm) through a chromium mask on a Karl Süss MJB Mask Aligner. The mask featured custom-designed patterns set in chromium on glass (Delta Mask, Netherlands). The patterns consisted of repeating 15x15 mm blocks of circular chambers with diameters ranging from 10 to 40 µm and triangular, pill-shaped and rectangular chambers with long axes/sides ranging from 15 to 200 µm. The UV-illumination crosslinked the SU8, which was further enhanced by a post-exposure bake of 15 min at 65^{o}C and 15 min at 95^{o}C, followed by gradual cooling. Unexposed SU8 was removed by immersing and sonicating the coverslip in a developer (Mr Dev 600, Microchem, Germany) for 2 minutes for shallow chambers (5 µm deep) and 10 minutes for deeper chambers. A final 30 min baking step at 150^{o}C was performed to prevent stress-related cracks in the SU8 film. The final chamber depth was measured with an Alpha-Step 500 Surface Profiler.

PDMS chamber lids. Microchambers were sealed with lids of polydimethylsiloxane (PDMS) rubber deposited on microscope slides. PDMS mixtures were prepared from a Sylgard 184 Silicone Elastomer Kit (Dow Corning, U.S.A.) with a 10:1 w/w base:curing agent ratio. Layers of PDMS with a uniform thickness of ~1 mm height were spincoated on 76x26 mm glass slides and cured in a preheated oven at 80^{o}C for 1 hour.

Surface Treatments. The chamber walls were passivated to prevent nonspecific adhesion of actin. PDMS lids were rendered hydrophilic with a corona discharge (BD-20V high frequency generator, Electro-Technic Products), which oxidizes the surface and produces silanol groups [2]. The oxidized PDMS lids were treated with PEG silane (2-[methoxy(polyethyleneoxy) propyl]-trimethoxysilane, ABCR) [3,4] for 2 hours and washed twice in water for 30 min prior to use. SU8 chambers were incubated with a 0.1 mg/mL kappa-casein (Sigma) solution for 15 min at room temperature. Excess kappa-casein was removed by washing with polymerization buffer and the chamber slide was dried with a stream of nitrogen.

Image Analysis

We analyzed fluorescence images of actin networks in chambers using a combination of MATLAB and ImageJ commands, including the ImageJ plugin OrientationJ (http://bigwww.epfl.ch/demo/orientation/), written by Daniel Sage at the Biomedical Imaging Group, EPFL, Switzerland. It was originally written to quantify the orientation of elastin fibers [5]. We briefly review OrientationJ before describing our techniques.

a) OrientationJ

This plugin quantifies the anisotropy of features found in an image of pixel intensities $I(x,y)$ (Fig S2A). Among its several outputs, we use the coherency $c(x,y)$ and orientation $\Theta(x,y)$ for our analysis. These quantities are derived from the structure tensor $J(x,y)$, defined by the spatial gradients of $I(x,y)$:

$$J(x,y) = \begin{bmatrix} \int_{ROI} dx\, dy\, \nabla_x I(x,y) \cdot \nabla_x I(x,y) & \int_{ROI} dx\, dy\, \nabla_x I(x,y) \cdot \nabla_y I(x,y) \\ \int_{ROI} dx\, dy\, \nabla_x I(x,y) \cdot \nabla_y I(x,y) & \int_{ROI} dx\, dy\, \nabla_y I(x,y) \cdot \nabla_y I(x,y) \end{bmatrix}$$

The region of interest (ROI) around each pixel of coordinates (x,y) is a Gaussian window with a user-defined width σ. This is the only input parameter, which should match the desired feature size. Diagonalizing the structure tensor J yields two eigenvalues λ_{min} and λ_{max} whose eigenvectors $\boldsymbol{\lambda}_{min}$ and $\boldsymbol{\lambda}_{max}$ point in the directions of minimum and maximum change in pixel intensity, respectively (Fig S2A, inset). The dominant orientation Θ of a region is given by the direction of $\boldsymbol{\lambda}_{min}$ (Fig S2B). The relative difference between λ_{min} and λ_{max}, called the coherency c, serves as a measure of a region's anisotropy (Fig S2C):

$$c = \frac{\lambda_{max} - \lambda_{min}}{\lambda_{max} + \lambda_{min}}$$

We rely on the coherency to quantify the presence of bundles in our images. OrientationJ furthermore produces a so-called "color survey" (Fig S2D): an RGB image where the orientation $\Theta(x,y)$ determines its hue, the coherency c(x,y) determines its saturation, and the original image intensity I(x,y) determines its brightness.

b) Bundle Parameter

Bundles in a labeled filamentous network can be detected by fluorescence microscopy based on two criteria: (i) they are brighter than the surrounding unbundled network, owing to the spatial condensation of filaments and (ii) they are long and thin, owing to the linear structure of the component filaments. We developed an algorithm to detect the presence of bundles in an image based on these two properties. For a pixel to belong to a bundle, we require that (i) it is brighter than background pixels and (ii) neighboring pixels' intensities vary slowly along the direction of the bundle but quickly in the orthogonal direction. Standard thresholds satisfy requirement (i), and the coherency output from OrientationJ satisfies requirement (ii). We combine these methods in a six-step process comprising ImageJ and MATLAB scripts, as summarized in Fig. S3. By processing many images, we produce an ensemble-averaged *bundle parameter B* for every geometrical and biochemical condition investigated. Briefly, we make for each fluorescence image a thresholded image and a coherence image. We then multiply these images to obtain an image in which bright pixels satisfy both requirements for bundling, and calculate the bundle parameter as the mean pixel intensity averaged over nonzero pixels. In detail, the 6 steps are the following:

1) **Crop:** We manually crop each image (Fig S3A) to the largest rectangle fitting inside the chamber (Fig S3B.1). This step avoids artifactual coherencies arising at the chamber edges (see Fig S2C).
2) **Bandpass Filter:** We apply the ImageJ "FFT Bandpass Filter" routine to the cropped image, to eliminate camera noise and uneven illumination (Fig S3B.2). This step introduces two input parameters that determine which spatial frequencies to preserve. We choose to remove features below 2 pixels (camera noise) and above 10 pixels (uneven illumination, blooming). Because bundles are typically ~5 pixels wide, their structure is preserved in the filter. If we eliminate the high-pass cutoff or make it too high, the thresholds in step 3 become inaccurate and start to pick up background pixels next to regions with many bundles that appear brighter due to blooming.
3) **Threshold:** We apply Yen's threshold method (Fig S3B.3) to the filtered image from step 2.
4) **Coherency:** We apply OrientationJ to the filtered image from step 2 and extract the coherency image (Fig S3B.4). This step introduces another input parameter which determines the width of the ROI around each pixel. We choose the typical bundle thickness of 5 pixels for this value.
5) **Multiply:** We multiply the images from step 3 and step 4, effectively masking the coherency image with the thresholded image (Fig S3B.5).
6) **Average:** We calculate the mean pixel intensity, averaged over nonzero pixels (Fig S3B.6). This mean defines the bundle parameter *B*.

The threshold in step 3 of the analysis has no variable input parameters, but the choice in algorithm does affect the analysis. Fig. S4A shows an extreme example of a chamber where the bundle parameter is very sensitive to the choice in threshold algorithm. In this image, the distinction between bundle and background is unclear. Some bundles are barely brighter than the surrounding background, even after bandpass filtering (Fig. S4B). A permissive threshold allows more low-coherency background pixels to pass, whereas a more restrictive threshold allows only the brightest pixels to pass, producing a more accurate mask in accordance with requirement (i).

We found that Otsu's method [6], a widely-used threshold algorithm, is fairly permissive and allows many background pixels to pass (Fig. S4C). More recent methods based on information theory more accurately separate bundles from the background. Kapur's method [7] maximizes the combined entropy of the pixel intensity distributions of the foreground and background, defined as $S = - \sum_{I=0}^{1} p(I) \log_2 p(I)$ (Fig S4D). Yen's method [8] minimizes a cost function that considers the discrepancy between the thresholded and original image along with the number of bits needed to represent the original image (Fig S4E). Fig. S4F (upper panel) shows how these thresholding algorithms affect the bundle parameter. In the absence of a threshold (black crosses), the bundle parameter does not change with gelsolin concentration, even though bundles are clearly visible in the original images (Fig. S4F lower panel). Otsu's method (gray circles) produces a slight increase in the bundle parameter with increasing gelsolin concentration. However, since this method averages over more background pixels and hence over more low-coherency pixels, it produces a lower bundle parameter than Kapur (red squares) and Yen's (yellow triangles) methods, especially for [gelsolin]:[actin]= 1:740. Kapur's and Yen's methods both give nearly identical thresholds and therefore nearly identical bundle parameters. Here we choose Yen's method, but choosing Kapur's method does not affect our results. The need for an

accurate threshold reflects a conscious design principle behind the bundle parameter: we consider only the coherency of pixels that pass the threshold, but do not normalize against chamber volume. Rather than characterizing volume fractions of bundles, we only seek to quantify the presence of bundles, reflected in requirements (i) and (ii) given above.

c) Test for edge accumulation of actin filaments

Our aim in this analysis is to quantify the spatial distribution of fluorescence intensity in each chamber. More specifically, we are interested in testing whether fluorescently labeled actin filaments accumulate at the chamber's periphery. We developed a five-step process comprising a MATLAB script (the "onion peel" algorithm). The result is a plot of fluorescence intensity as a function of distance from the center for each chamber. Briefly, we threshold the entire image of a chamber to find its boundary, and "peel" away layers from this threshold. Pixels of the same peel are equally distant from the chamber boundary/center. We then separate the original image into a series of peels and plot the mean intensity of each peel against the distance from the chamber center. We now present each step in more detail:

- **Median filter:** We median filter the original image (Fig S5A) with a circular kernel of radius 10 pixels (Fig S5B.1). We choose this filter because it smoothes the image but preserves edges, which is necessary to detect chamber boundaries.
- **Threshold:** We apply Otsu's threshold method to the filtered image (Fig S5B.ii). Kapur's and Yen's methods (Fig S5B.iii and iv, respectively) capture details inside the chamber but not its boundary. Otsu's method applied to the original image also results in an inaccurate threshold (Fig S5B.v).
- **Erode and Subtract:** We erode the threshold by one pixel and subtract the result to recover a ring of pixels corresponding to the chamber's boundary (Fig S5B.vi, "onion skin"). We loop this process, where each iteration j yields a series of images (Fig S5B.vii,viii, "peels"), until we reach the center of the chamber (Fig S5B.ix, "onion core"). Eroding this final image would yield a dark image with no white pixels. We convert loop iteration j into a dimensionless distance from the confining boundary by dividing j by the total number of iterations j_{tot} (j_{tot} = 58 for Fig S5). We furthermore define a dimensionless distance from center, r/r_c, normalizing r by the chamber's "radius" r_c. Note that r and r_c correspond to real radii for circular chambers, whereas for pill-shaped chambers, r corresponds to a minimum distance from the "onion core" (Fig. S5B.ix).
- **Multiply:** We multiply each onion peel with the original image, yielding a series of images (Fig. S5B.x-xiii) which decompose the original image into equivalence classes based on distance from boundary. Because each pixel corresponds to only one onion peel, the original image is faithfully represented in the series of images resulting from this step.
- **Mean:** We compute the mean intensity I of the intensity distribution of every peel, averaged over nonzero pixels, as in Fig S5C. Because each peel comprises hundreds of pixels, we do not require spatial filtering to eliminate camera noise. However, because there are fewer pixels in each peel as r tends to 0, the noise increases as r/r_c goes to 0 (this is clearly visible in Fig. 6 of main text). We furthermore compute the median intensity I_m of the chamber, defined as the product between the original image (Fig S5A) and the threshold (Fig S5B,ii), and normalize I by I_m (Figb S5B.x-xiii, lower right). We choose to normalize against the median as opposed to the mean because of a systematic decrease in intensity as r/r_c tends to 1. This decrease corresponds to a diffuse, diffraction-

limited boundary between chamber and background. The median is insensitive to this systematic decrease.

- Finally, we plot I/I_m as a function of r/r_c (Fig. S5C and inset of Fig. S5C).

Support Figure Captions

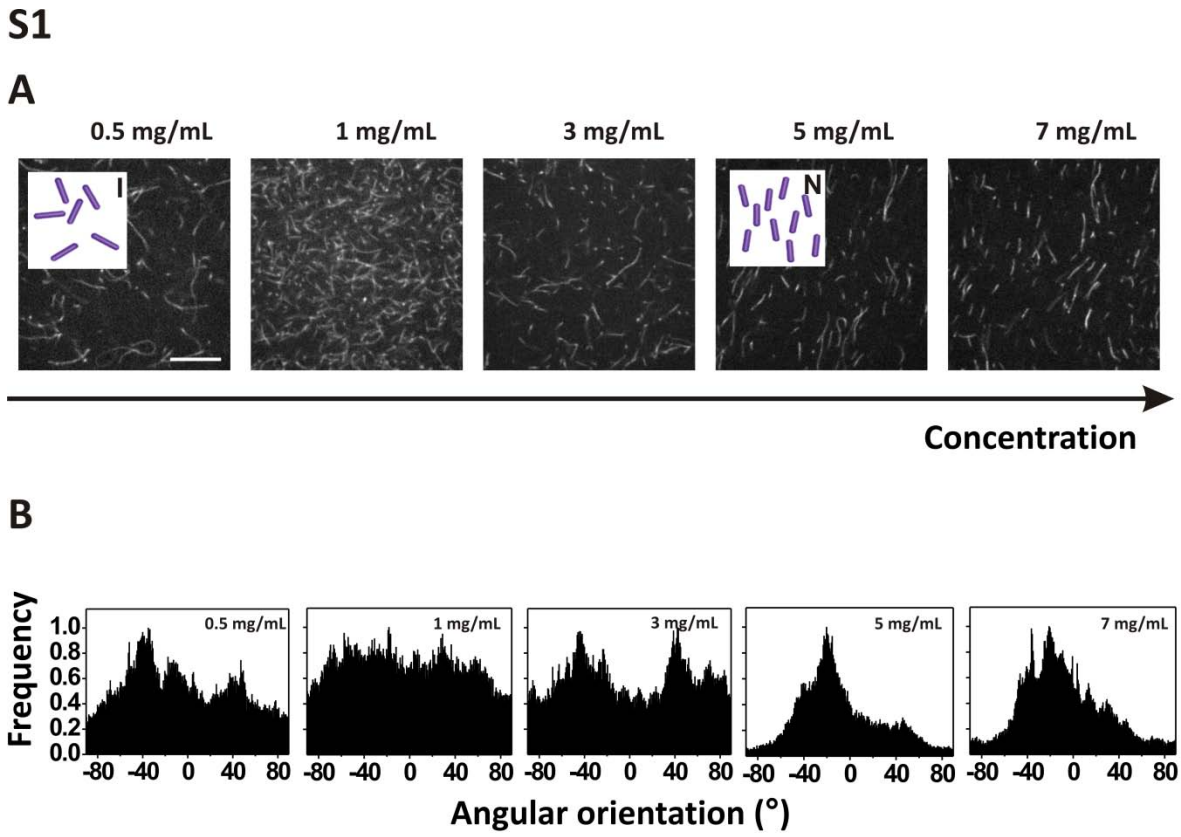

Figure S1. Fluorescent actin filaments embedded in a dark F-actin network display orientational alignment above a threshold concentration of 5 mg/ml. (**A**) Fluorescent confocal micrographs of tracer actin filaments labeled with 30 mol% Alexa488-G-actin and stabilized with 1:1 phalloidin, embedded in unlabeled networks of 0.5-7 mg/mL F-actin. There is 1 fluorescent filament per 500 nonfluorescent filaments. Insets show schematics of an isotropic distribution of rod-like particles (I) and nematically ordered (N) rods. Scale bar is 10 μm. (**B**) Histograms of the orientation angles of image pixels corresponding to the images in (A).

S2

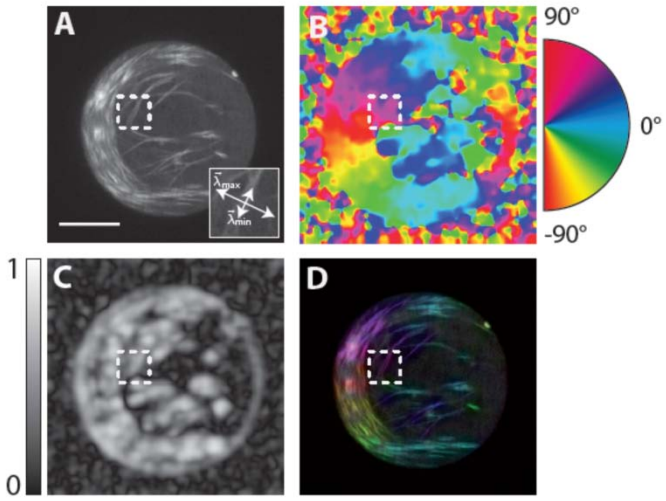

Figure S2. Procedure for determination of pixel coherency and orientation with OrientationJ. (**A**) Example input image (x,y) of a fluorescently labeled actin network confined to a microchamber. Actin concentration is 3 mg/mL, gelsolin/actin molar ratio is 1:370, chamber diameter is 40 µm, and chamber depth is 5 µm. Scale bar 10 µm. Inset: Close-up of dashed box in (A), with the eigenvectors λ_{min} and λ_{max} of the center pixel's structure tensor J. Note that λ_{min} points in the direction of the center bundle. (**B**) Orientation $\Theta(x,y)$ of (A), where pixel hues map to Θ according to the legend (right). (**C**) Coherency $c(x,y)$ of (A), where pixel intensities map to c according to the calibration bar (left). (**D**) Color survey of (A).

S3

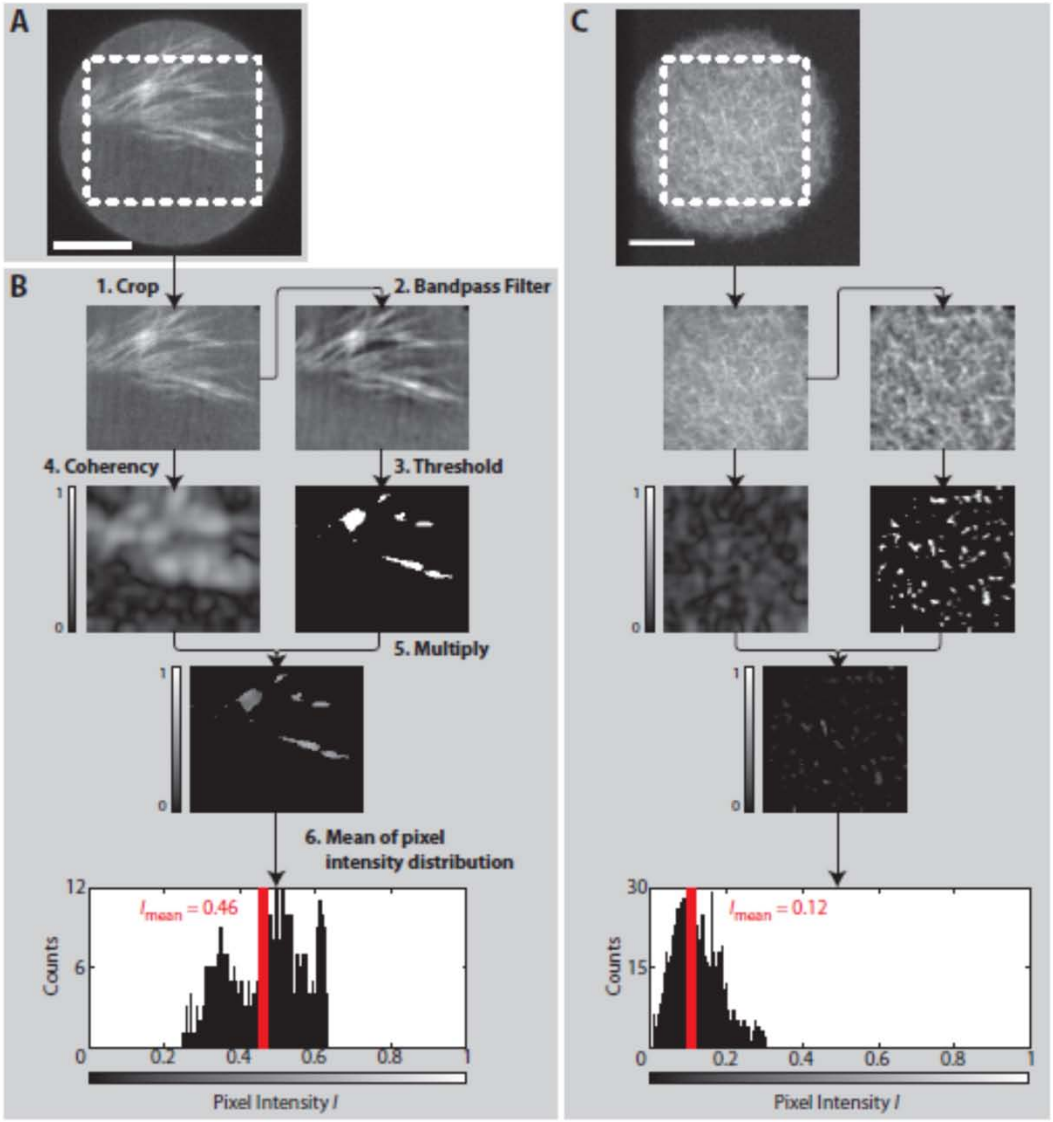

Figure S3. Procedure for determination of bundle parameter. (**A**) Example input image of chamber with bundles (5 mg/mL actin, 1:370 gelsolin/actin, chamber diameter 30 µm, chamber depth 5 µm). (**B**) Six-step algorithm for processing images. Step 1: crop to the largest rectangle fitting inside the chamber (a, dashed box). Step 2: bandpass filter. Step 3: threshold with Yen's method. Step 4: coherency of filtered image from step 2. Pixel intensity scale is indicated by calibration bar, right. Step 5: multiply images from steps 3 and 4. Pixel intensity scale is indicated by calibration bar, right. Step 6: mean of intensity distribution of nonzero pixels from step 5. Red bar denotes mean intensity, which is taken as the bundle parameter. Lower calibration bar corresponds to (5). (**C**) Example input image and output for a chamber with a homogeneous actin network with no bundles (0.5 mg/ml actin, chamber diameter 30 µm, chamber depth 5 µm). Scale bars, 10 µm.

S4

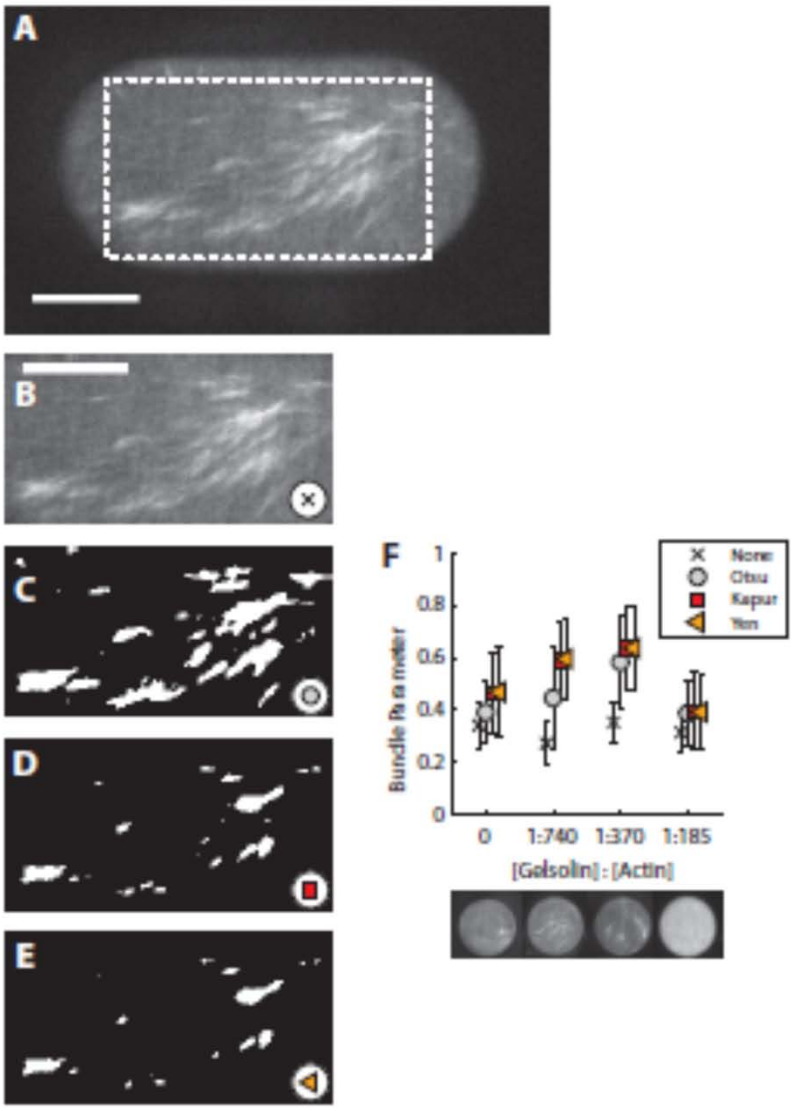

Figure S4. Dependence of bundle parameter on thresholding method. (**A**) Sample input image for a chamber with xy-dimensions of 60 μm × 30 μm and depth of 5 μm, containing 5 mg/mL actin and 1:740 gelsolin/actin. (**B**) Bandpass-filtered image of cropped area corresponding to dashed box in (A). (**C**-**E**) Thresholded image of (B) after bandpass filtering, according to the methods of Otsu (C), Kapur (D), and Yen (E). (**F**) Dependence of bundle parameter on thresholding method for actin networks of 5 mg/mL in pill-shaped chambers with 4 different gelsolin concentrations. Black crosses refer to no thresholding, gray circles refer to Otsu's method, red squares to Kapur's method, yellow triangles to Yen's method. Error bars indicate standard deviations of ensemble averages over (from left to right): N = 177, 43, 70, and 48 chambers. Lower panel: unprocessed representative images of each condition for chambers with a diameter of 40 μm and depth of 5 μm. Scale bar 10 μm.

S5

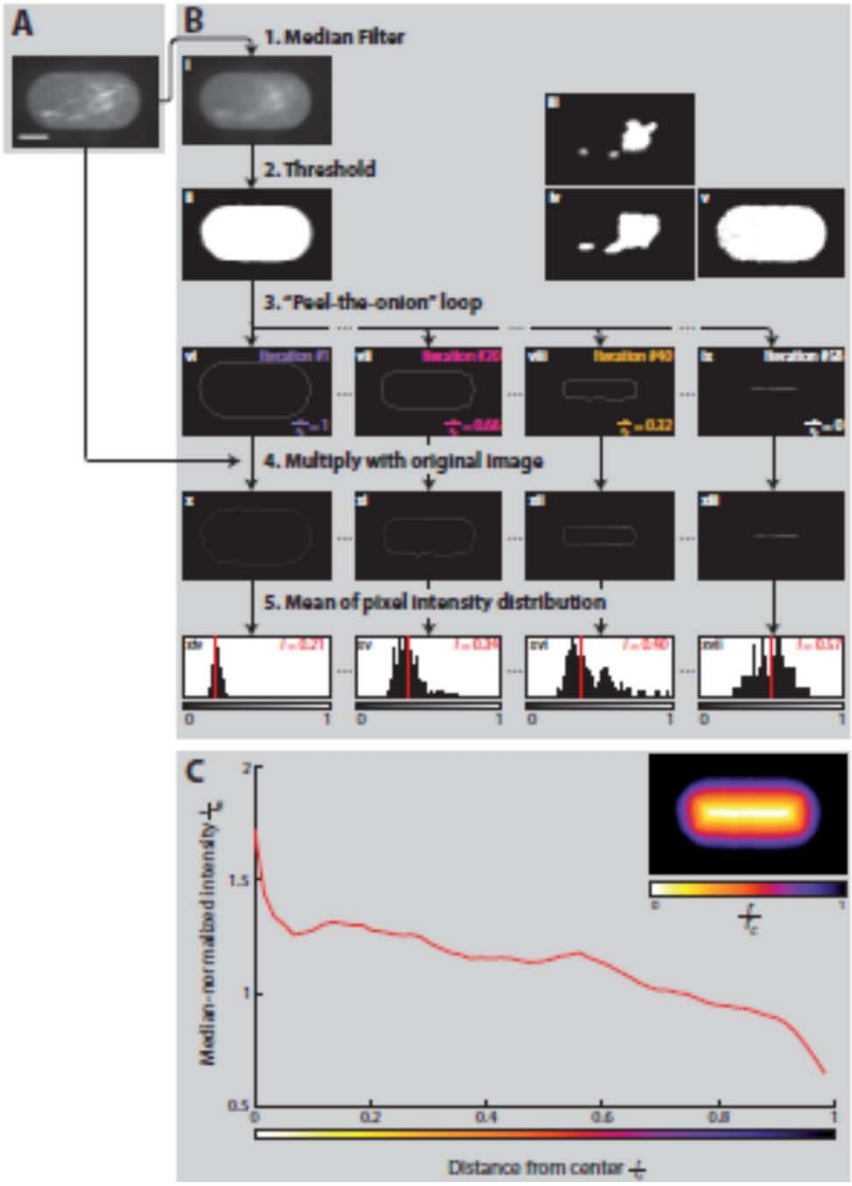

Figure S5. Procedure for analysis of actin accumulation at the chamber edge ("onion peel algorithm"). (**A**) Example input image of a 5 mg/ml actin network (with 1:740 gelsolin/actin) in a chamber with xy-dimensions of 60 × 30 μm and depth of 5 μm. Scale bar 10 μm. (**B**) Five-step algorithm for processing images. i. Step 1: median filter. ii-iv. Step 2: threshold with the method of Otsu (ii). For comparison, we show thresholded images obtained with methods of Kapur (iii) and Yen(iv), which do not return the chamber edge. v. Otsu threshold of the original image (A) instead of the median-filtered image also does not correctly identify the chamber edge. vi-ix. Step 3: "onion peels" corresponding to loop iteration j=1 (vi, "onion skin"), 20 (vii), 40 (viii), and 58 (ix, "onion core"). x-xiii. Step 4: multiply "onion peels" with original image (A). xiv-xvii.

Step 5: mean value I of the intensity distribution of nonzero pixels, normalized by the median value I_m (vi-ix, bottom right). (**C**) Plot of I/I_m versus r/r_c. Calibration bar underneath the x-axis corresponds to the color labels of the onion peels in panels (B vi-ix). Inset combining all 58 images from step 3 and shading according to iteration j yields a level set. Pixel color map is shown in the lower bar and corresponds to the bar underneath the x-axis of the graph.

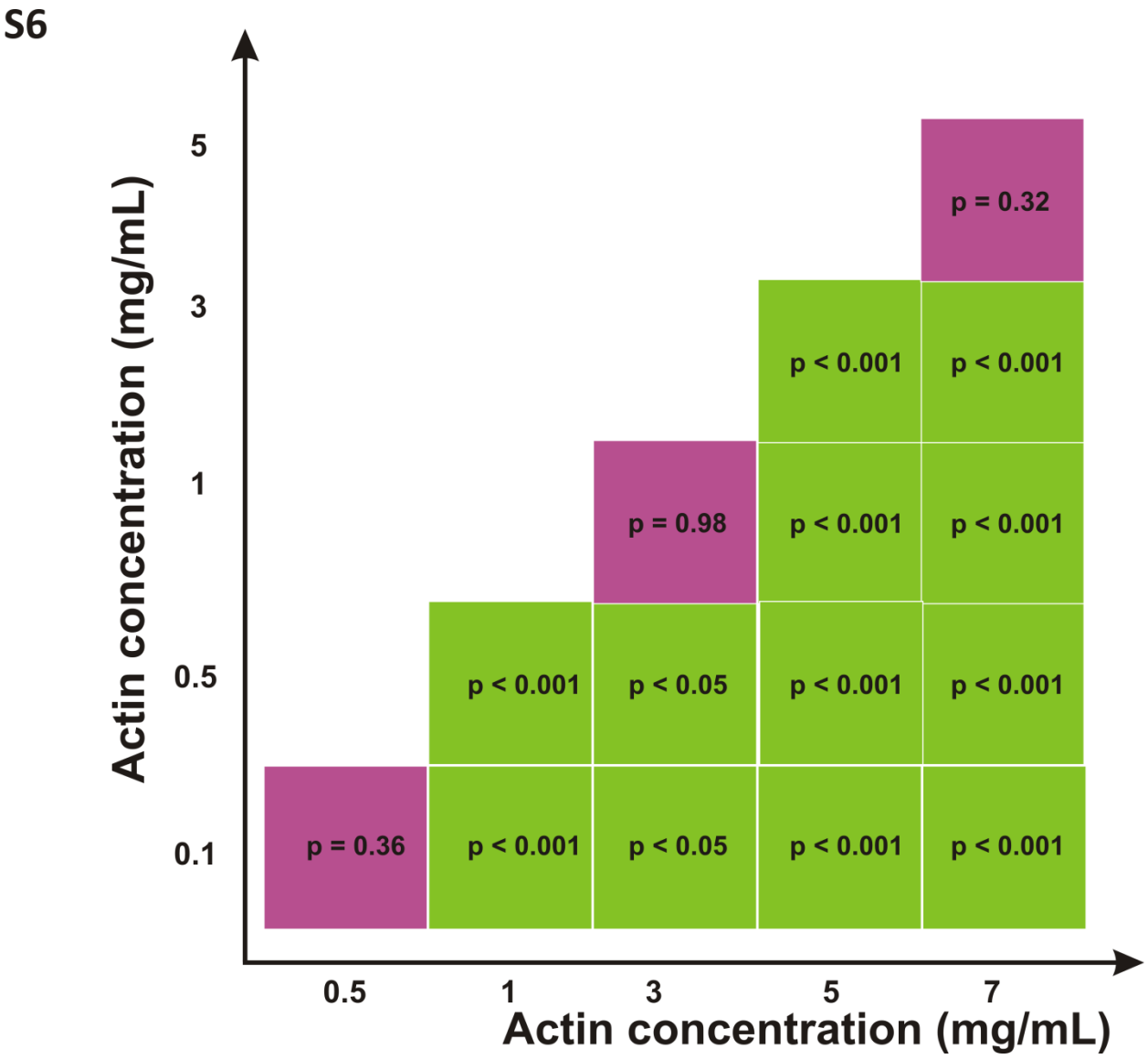

Figure S6. Statistical significance of differences between bundle parameters *B* of actin networks of different concentrations confined in circular chambers. Green boxes refer to pairs which are significantly different ($p<0.001$) and purple boxes refer to pairs which are not significantly different (p-value shown in box). Dilute samples of 0.5 mg/ml actin (which look homogeneous in confocal micrographs and have *B*-values around 0.2) are significantly different from dense acti samples (1-7 mg/ml) which show bundles and have *B*-values of 0.5-0.6. T-student statistical tests were performed on ensemble averages of 8-81 chambers per experimental condition, averaging over circular chambers of all diameters.

S7

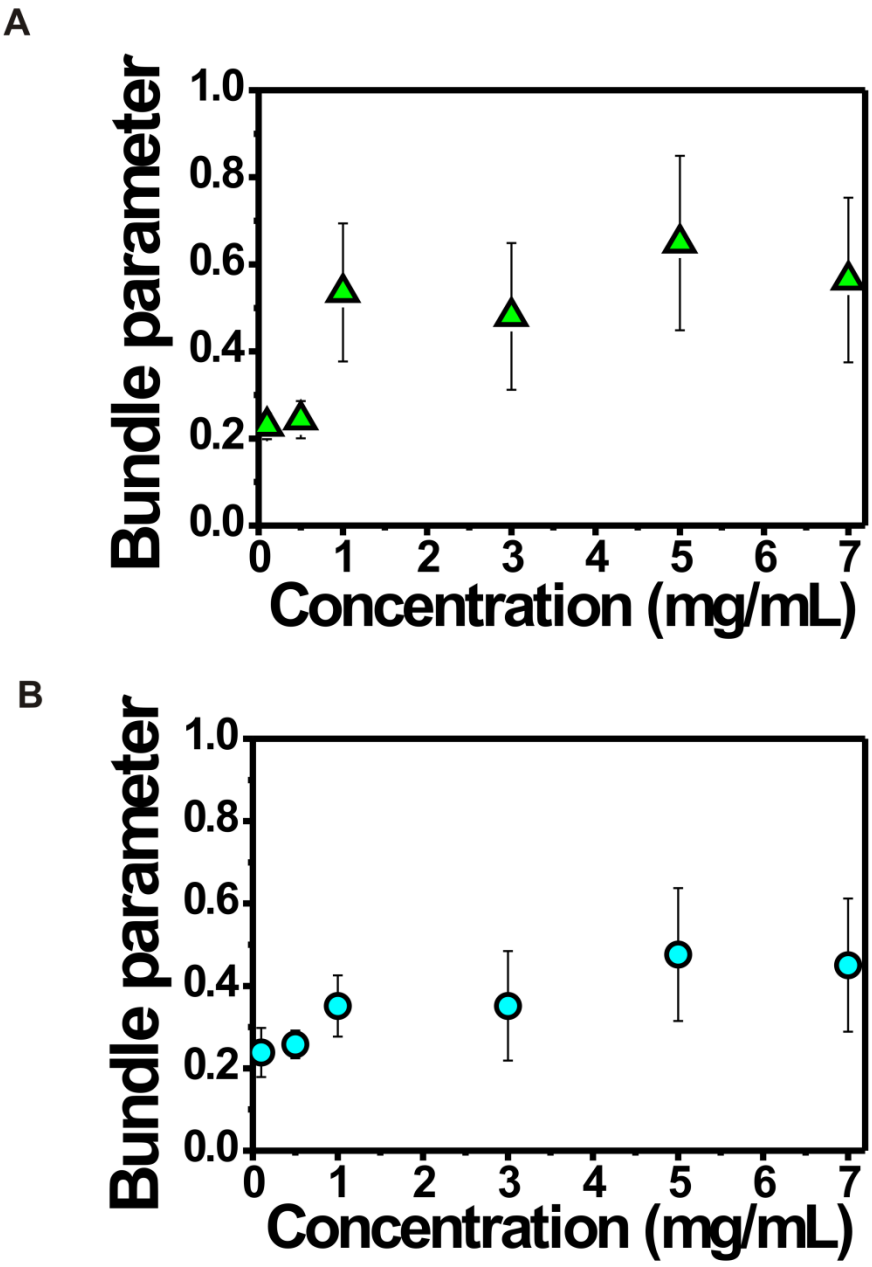

Figure S7. Increasing actin concentration inside microchambers leads to bundling above 1 mg/ml irrespective of chamber shape. (**A**) Bundle parameter for confined actin networks inside 30 μm hypotenuse triangles versus actin concentration. (**B**) Bundle parameter for confined actin networks inside circular chambers averaged over all sizes (10-30 μm diameter) versus actin concentration. Error bars represent S.D. of the mean.

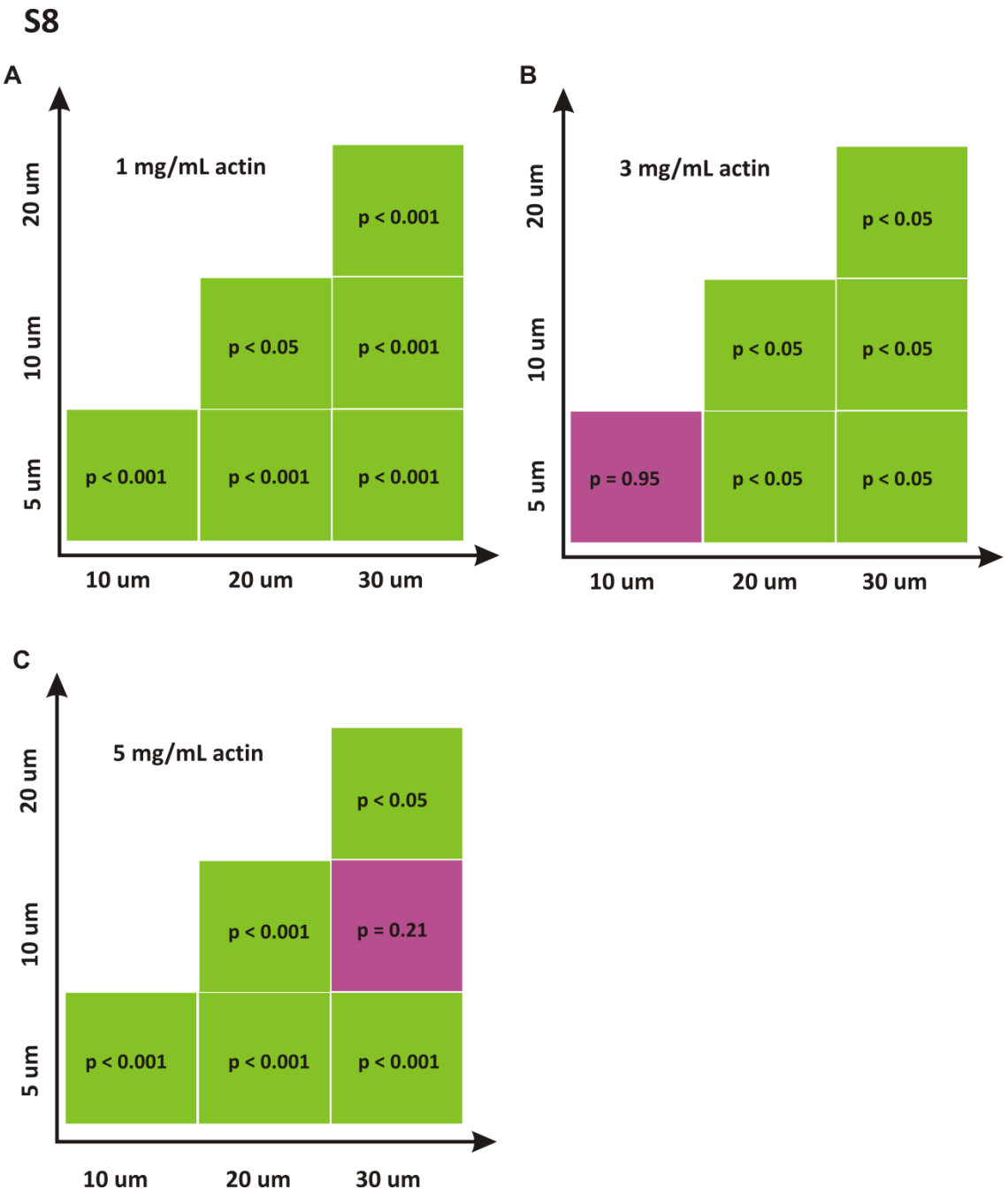

Figure S8. Statistical significance of differences between bundle parameters *B* of actin networks with concentrations of 1, 3 or 5 mg/ml in shallow chambers (5 μm depth) compared to deeper chambers (10-30 μm depth). Green boxes refer to pairs which are significantly different ($p<0.05$ or $p<0.001$) and purple boxes refer to pairs which are not significantly different (p-value shown in box). *B* in shallow chambers is significantly higher than in deep chambers, except for 3 mg/ml actin in 10 μm deep chambers. T-student statistical tests were performed on ensemble averages of 3-273 chambers per experimental condition, averaging over pill-shaped chambers of varying aspect ratio (1:1 – 4:1) and minor dimension (10-40 μm).

S9

A

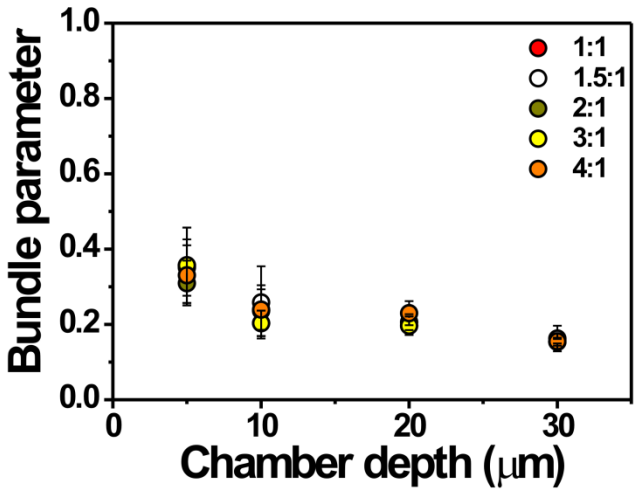

B

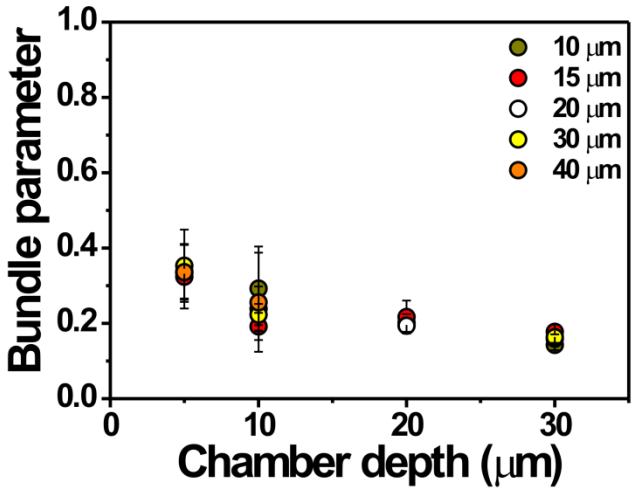

Figure S9. Increasing depth of microchambers leads to loss of bundling in confined actin networks (1 mg/ml), irrespective of chamber shape or size. (**A**) Bundle parameter for confined actin networks in pill-shaped chambers of increasing depth, for different in-plane aspect ratios. (**B**) Bundle parameter for confined actin networks in circular chambers of increasing depth, for different chamber diameters. Error bars represent S.D. of the mean.

S10

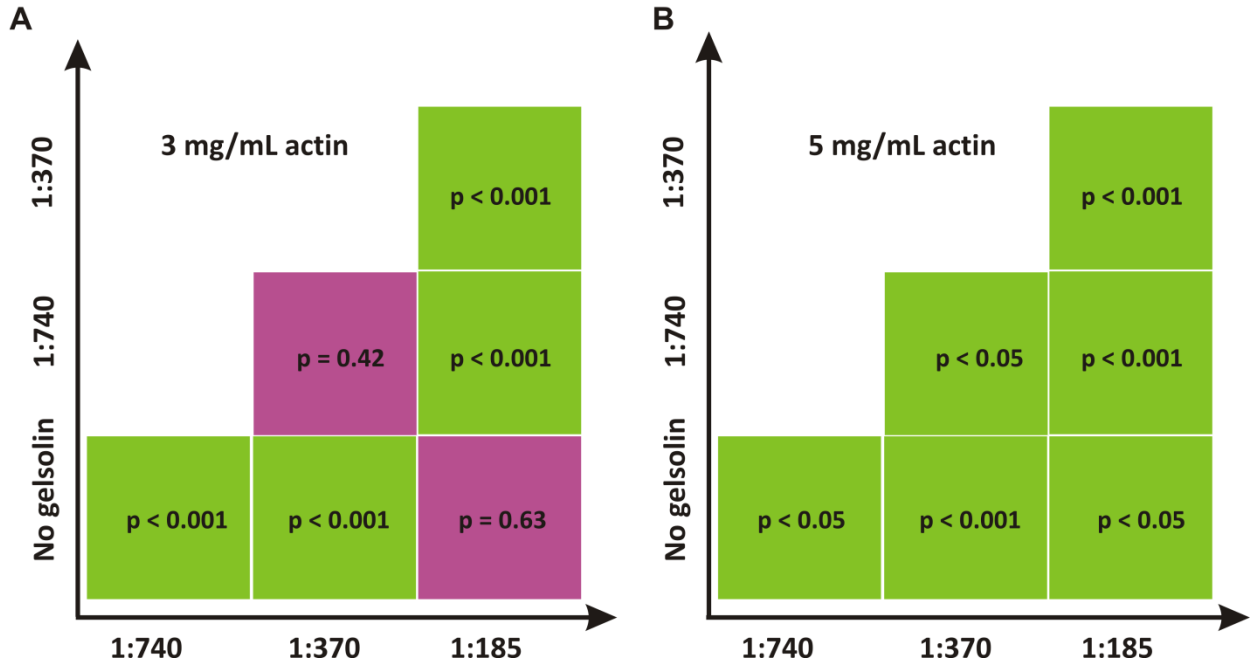

Figure S10. Statistical significance of differences between bundle parameters *B* of actin networks in shallow chambers (5 μm depth) in the presence of different concentrations of gelsolin. Data are shown for 3 mg/ml actin (left) and 5 mg/ml actin (right). Nearly all pairs show significant differences (green boxes, $p<0.05$ or $p<0.001$). This implies that adding gelsolin to an actin network causes a statistically significant increase of *B* up to a 1:370 gelsolin:actin ratio, while causing a decrease of *B* when added in a 1:185 gelsolin:actin ratio. T-student statistical tests were performed on ensemble averages of 38-264 chambers per experimental condition, averaging over pill-shaped chambers of varying aspect ratio (1:1 – 4:1) and minor dimension (10-40 μm).

S11

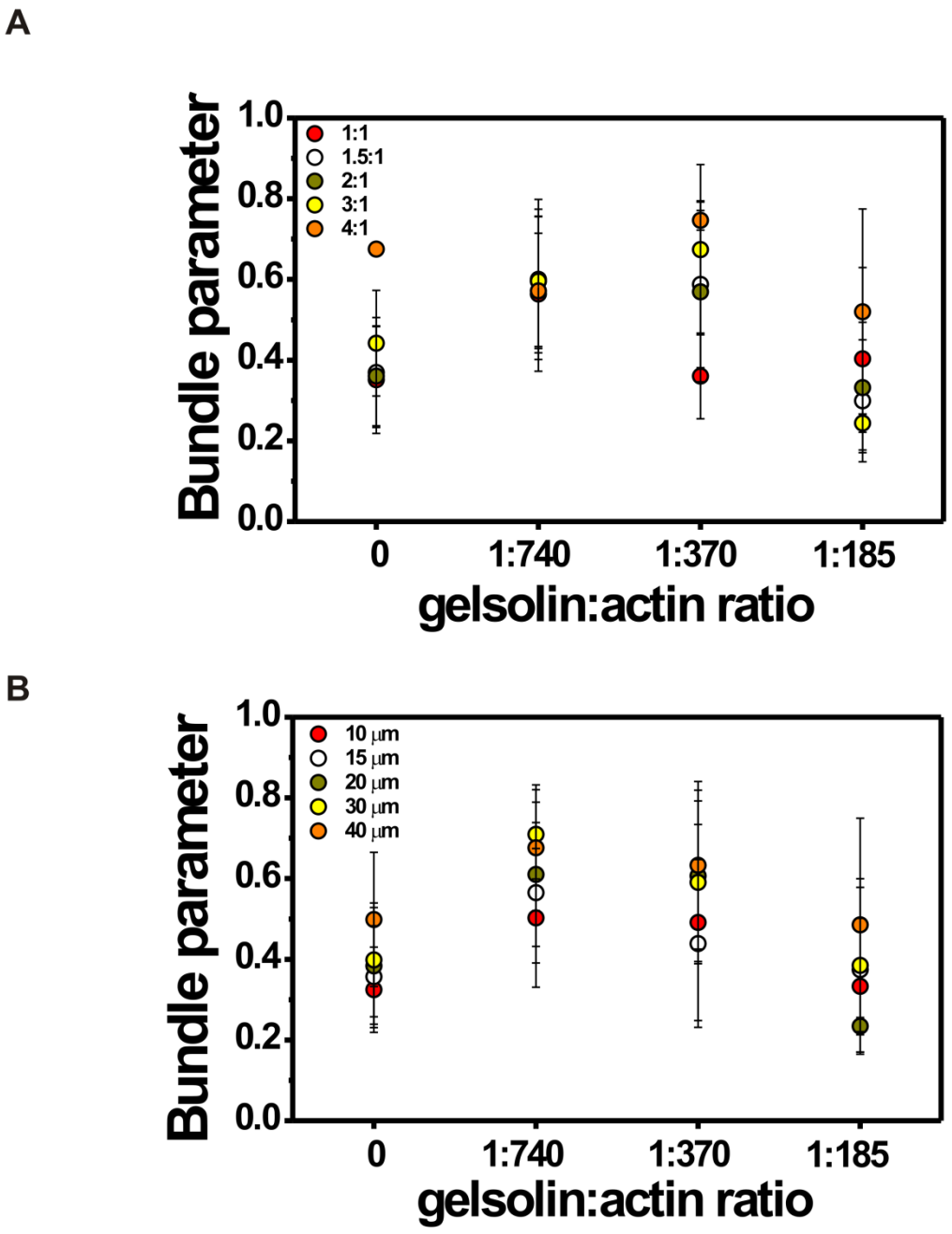

Figure S11. Increasing the gelsolin/actin molar ratio from zero to 1:185 for networks of 3 mg/ml actin causes an increase and then a decrease in bundling, irrespective of chamber shape or size. (**A**) Bundle parameter for confined actin networks in pill-shaped chambers of different in-plane aspect ratios. (**B**) Bundle parameter for confined actin networks in circular chambers of different diameters. Error bars represent S.D. of the mean.

References

[1] T. A. Anhoj, A. M. Jorgensen, D. A. Zauner, en J. Hubner, in *Micromachining Technology for Micro-Optics and Nano-Optics IV*, bewerkt door E. G. Johnson, G. P. Nordin, en T. J. Suleski (SPIE, 2006), p. 611009.

[2] H. Hillborg en U. W. Gedde, Polymer **39**, 1991-1998 (1998).

[3] V. Sharma, M. Dhayal, Govind, S. M. Shivaprasad, en S. C. Jain, Vacuum **81**, 1094-1100 (2007).

[4] W. Hellmich, J. Regtmeier, T. T. Duong, R. Ros, D. Anselmetti, en A. Ros, Langmuir **21**, 7551-7557 (2005).

[5] E. Fonck, G. G. Feigl, J. Fasel, D. Sage, M. Unser, D. A. Rufenacht, en N. Stergiopulos, Stroke **40**, 2552-2556 (2009).

[6] N. Otsu, Systems, Man and Cybernetics, IEEE Transactions on DOI - 10.1109/TSMC.1979.4310076 **9**, 62-66 (1979).

[7] J. N. Kapur, P. K. Sahoo, en A. K. C. Wong, Computer Vision, Graphics, and Image Processing **29**, 273-285 (1985).

[8] Jui-Cheng Yen, Fu-Juay Chang, en Shyang Chang, Image Processing, IEEE Transactions on DOI - 10.1109/83.366472 **4**, 370-378 (1995).